Received: 11 February 2020 | Revised: 30 June 2020 | Accepted: 14 July 2020

DOI: 10.1002/mrm.28462

FULL PAPER

Magnetic Resonance in Medicine

A 3D hybrid-shot spiral sequence for hyperpolarized ^{13}C imaging

Andrew Tyler[1,2] | **Justin Y. C. Lau**[1,2] | **Vicky Ball**[1] | **Kerstin N. Timm**[1] | **Tony Zhou**[1,2] | **Damian J. Tyler**[1,2] | **Jack J. Miller**[1,2,3]

[1]Department of Physiology, Anatomy & Genetics, Sherrington Building, Parks Road, University of Oxford, Oxford, OX1 3PT, United Kingdom

[2]Oxford Centre for Clinical Cardiac Magnetic Resonance Research (OCMR), Level 0, John Radcliffe Hospital, Headley Way, Headington, OX3 9DU, United Kingdom

[3]Department of Physics, Clarendon Laboratory, University of Oxford, Parks Road, Oxford, OX1 3PU, United Kingdom

Correspondence
Jack J. Miller, Sherrington Building, Parks Road, Oxford, OX1 3PT, United Kingdom.
Email:jack.miller@physics.org

Funding information
Engineering and Physical Sciences Research Council (EPSRC) and Medical Research Council (MRC) joint ref., Grant/Award Number: EP/L016052/1; British Heart Foundation refs, Grant/Award Number: FS/14/17/30634 and RE/13/1/30181

Purpose: Hyperpolarized imaging experiments have conflicting requirements of high spatial, temporal, and spectral resolution. Spectral-spatial RF excitation has been shown to form an attractive magnetization-efficient method for hyperpolarized imaging, but the optimum readout strategy is not yet known.

Methods: In this work, we propose a novel 3D hybrid-shot spiral sequence which features two constant density regions that permit the retrospective reconstruction of either high spatial or high temporal resolution images post hoc, (adaptive spatiotemporal imaging) allowing greater flexibility in acquisition and reconstruction.

Results: We have implemented this sequence, both via simulation and on a preclinical scanner, to demonstrate its feasibility, in both a ^{1}H phantom and with hyperpolarized ^{13}C pyruvate in vivo.

Conclusions: This sequence forms an attractive method for acquiring hyperpolarized imaging datasets, providing adaptive spatiotemporal imaging to ameliorate the conflict of spatial and temporal resolution, with significant potential for clinical translation.

KEYWORDS

DNP, hyperpolarized ^{13}C, metabolic imaging, pulse sequence design, spectral-spatial RF, spiral imaging

1 | INTRODUCTION

Hyperpolarized [1-^{13}C] is a versatile metabolic probe, which has been used extensively to investigate metabolism and pH in health and disease in vivo,[1-3] and is progressing rapidly toward clinical translation.[4-9] Many conditions where metabolic dysregulation is of interest are spatially localized; therefore, it would be desirable to image at sufficiently high spatial resolution to appreciate potential metabolic heterogeneities within the tissue, for instance, in the myocardium post infarction to assess viability when planning intervention. It is also desirable to perform time-resolved imaging to observe temporal metabolic dynamics, which may be significantly altered in

Damian J. Tyler and Jack J. Miller contributed equally to this work.

pathology, for instance, in ischemic cardiomyopathies.[10] Furthermore, a growing body of work advocates for the use of time-course data for the determination of metabolic parameters, such as k^{PL} (pyruvate-lactate), either via the fitting of kinetic models[11,12] or calculation of area-under-the-curve ratios,[13] necessitating high-quality time-courses with sufficient temporal resolution to properly characterize the shape of the curve. In addition, owing to the inherent physiological variability in the time between the injection of hyperpolarized pyruvate and its arrival in the organ of interest, the use of dynamic imaging strategies is preferred, to ensure that the acquisition does not miss the initial bolus of injected substrate.[14] It is therefore desirable to have both high spatial and temporal resolution in the same acquisition, in practice, there is a trade-off between spatial and temporal resolution, which thus far must be predefined a priori at the time of acquisition.

The finite, decaying, and non-renewable magnetization generated by hyperpolarization necessitates rapid, magnetization-efficient imaging techniques. One common strategy is to combine the magnetization efficiency of spectral-spatial RF excitations with rapid spiral readouts.[15-20] The first hyperpolarized ^{13}C images of the human heart were acquired with a single-shot spiral trajectory.[5] Single-shot spiral-out readouts efficiently encode a plane of k-space with minimal dead time by starting at the center of k-space with the energy-rich low spatial frequencies. However, for a given field of view (FOV), the maximum spatial resolution that can be achieved with a single-shot spiral is limited by the readout duration allowed by the magnetic field inhomogeneity of the sample[21] and the T_2^* of the hyperpolarized nuclei in question.

One approach to overcome the limiting effect of T_2^* is to use a multi-shot spiral readout,[22] which segments the acquisition of k-space into multiple readouts, each temporally shorter and therefore less affected by T_2^* decay than an equivalent single-shot spiral readout. However, as each segment does not typically meet the Nyquist criterion, it is not possible to reconstruct images individually from each interleaf at the prescribed FOV without aliasing. Another strategy to shorten the readout is to design variable density spiral (VDS) trajectories,[23] where the sampling density is not constant across k-space. Spiral-out VDS designs with a sampling density that decreases as a function of the distance away from the center of k-space have been used to reduce artifacts due to motion[24] and aliasing.[25] However, there is a penalty in the signal-to-noise ratio associated with VDS designs due to noise amplification from the weighting of the varying sampling density in the image reconstruction process.

In this work, we demonstrate the feasibility of adaptive spatiotemporal imaging using a hybrid-shot spiral (HSS) trajectory which features a constant single-shot density inner region to satisfy the Nyquist criteria up to a minimum desired spatial resolution, followed by a smooth transition to a constant N-shot density sub-Nyquist outer region. By truncating each readout to the inner single-shot region (single-shot HSS), low spatial resolution images can be reconstructed for each TR. By combining non-truncated data which encompass a full set of rotation angles from N acquisitions of the same metabolite, alias-free higher spatial resolution images can be reconstructed (full HSS) at lower temporal resolution. This adaptive spatiotemporal feature of the HSS acquisition allows the trade-off between spatial and temporal resolution to be made post hoc at reconstruction time.

2 | THEORY

Numerous strategies for designing spiral trajectories exist in the literature. Given upper limits for gradient amplitude and slew rate, analytical formulae can be derived to design constant density[26] and variable density[27] spiral trajectories. A hybrid-density trajectory has been proposed for functional MRI with a single-shot inner region up to a fraction of the maximum design k-space radius beyond which the sampling density decreases.[28] In this work, the target HSS trajectory (shown in Figure 1) consists of two connected regions of constant sampling density with a transition that is smooth but relatively abrupt as opposed to a gradual change in sampling density common with VDS designs using the aforementioned algorithms.

Iterative algorithms compute each point of the trajectory by solving a coupled set of differential equations with the previous point as the initial condition. A widely used example of an iterative VDS design algorithm represents the sampling density as an effective FOV, which is a function of k-space radius.[29,30] In this algorithm, the spiral trajectory is defined as

$$\mathbf{k} = a\theta e^{i\theta} \tag{1}$$

where $\mathbf{k} = k_x + ik_y$, θ is the polar angle and a is the rate of increase of k-space radius ($k_r = |\mathbf{k}|$) with respect to θ, which is defined by

$$a = \frac{dk_r}{d\theta} = \frac{N\Delta k_{max}}{2\pi} = \frac{N}{2\pi \cdot FOV} \tag{2}$$

If FOV is allowed to vary as a function of k-space radius, a variable density spiral can be constructed. Differentiating Equation (1) gives an equation for the gradient vector ($\mathbf{G}$)

$$\mathbf{G} = \frac{2\pi a}{\gamma} e^{i\theta}(\dot{\theta} + i\theta\dot{\theta}) \tag{3}$$

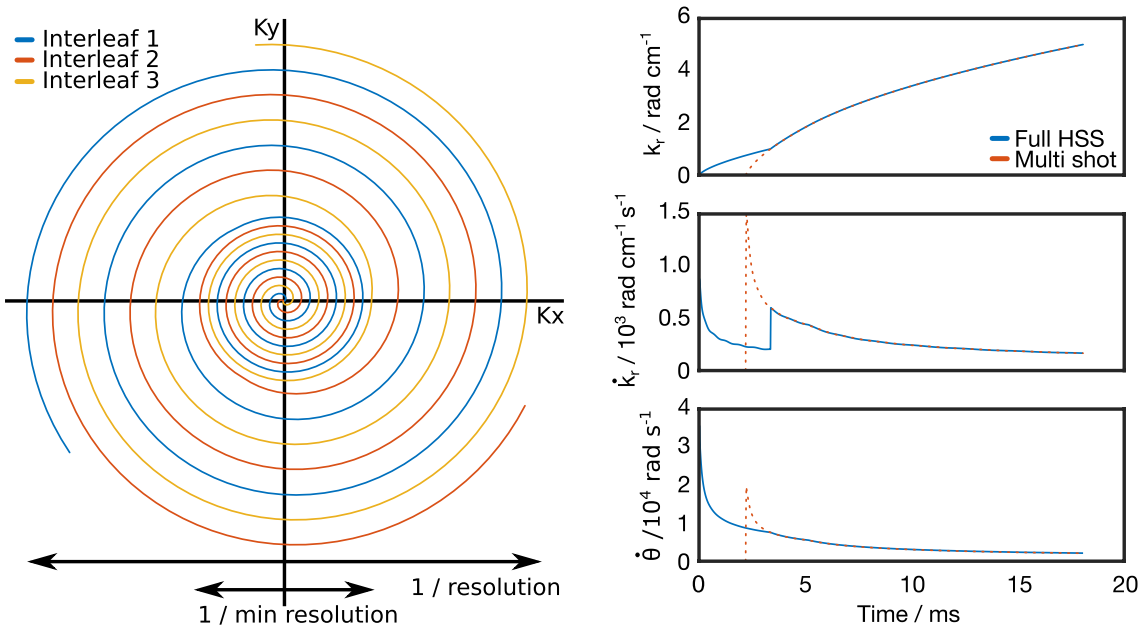

FIGURE 1 Left: The proposed k-space readout trajectory (experimental parameters as in the digital phantom experiment). In this case, three shots are required for a full resolution reconstruction; however an image can be reconstructed every shot at a lower spatial resolution. Right: k_r, $\dot{k}_r$ and $\dot{\theta}$ values as a function of time for the shown trajectory superimposed with an aligned multi-shot spiral with the same imaging parameters

which can be further differentiated to give an equation for the slew rate (**S**)

$$\mathbf{S} = \frac{2\pi a}{\gamma} e^{i\theta}[(\ddot{\theta} - \theta\dot{\theta}^2) + i(2\dot{\theta}^2 + \theta\ddot{\theta})] \tag{4}$$

By taking the magnitude of Equation (3) and setting $|\mathbf{G}| = G_{\max}$, the gradient limited value of $\dot{k}_r$ can be found

$$\dot{k}_{\max} = \sqrt{\frac{(\gamma G_{\max})^2/4\pi^2}{1 + \left(\frac{k_r}{a}\right)^2}} \tag{5}$$

Similarly, solving Equation (4) in the same way, gives an expression for the slew rate limited ($|\mathbf{S}| = S_{\max}$) value of $\ddot{k}_r$

$$\ddot{k}_{\max} = \frac{-B}{2A} + \sqrt{\frac{B^2}{4A^2} - \frac{C}{A}} \tag{6}$$

where A, B, and C are the quadratic coefficients used to solve the equation

$$A = 1 + \frac{k_r^2}{a^2} \tag{7}$$

$$B = \frac{2k_r\dot{k}_r^2}{a^2} \tag{8}$$

$$C = \left(\frac{k_r \cdot \dot{k}_r^2}{a^2}\right)^2 + \frac{4\dot{k}_r^4}{a^2} - \gamma^2 S_{\max}^2/4\pi^2 \tag{9}$$

This gives the following equation for $\ddot{k}_r$, subject to the dual constraints of $G_{\max}$ and $S_{\max}$

$$\ddot{k}_r = \begin{cases} \ddot{k}_{\max} & \dot{k}_r < \dot{k}_{\max} \\ \left(\dot{k}_{\max} - \dot{k}_r\right)/\Delta t & \dot{k}_r \geq \dot{k}_{\max} \end{cases} \tag{10}$$

where Δt is the scanner dwell time. $\ddot{\theta}$ can then be found with the expression

$$\ddot{\theta} = \frac{1}{a} \cdot \ddot{k}_r \tag{11}$$

To calculate the trajectory, $\dot{\theta}$ and $\dot{k}$ are incremented by $\ddot{\theta}$ and $\ddot{k}$ at each timepoint with θ and k also incremented at each timepoint by the new values of $\dot{\theta}$ and $\dot{k}$. All variables are initialized to 0 at the first timepoint and the algorithm is terminated when k_r reaches the value corresponding to the desired resolution.

The iterative algorithm was modified to design HSS trajectories with a transition from single-shot to N-shot sampling density at a k-space radius corresponding to the desired minimum resolution for a high temporal resolution reconstruction. In its modified form, the algorithm begins as for a single-shot spiral, then once the trajectory reaches the k-space radius corresponding to the single-shot HSS resolution, k_{trans}, the FOV parameter is scaled by a factor of $1/N$, reducing the sampling density to that of a N-shot spiral, until the end of the readout. At the transition between the two density regions, $\dot{k}_r$ is set equal to $\dot{k}_{\text{trans}}$, the value of $\dot{k}_r$ for an N-shot spiral at k_{trans}. The algorithm is now in a

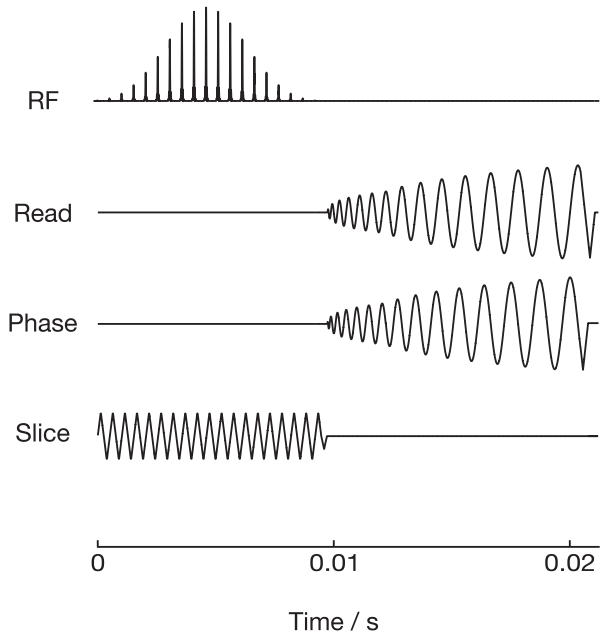

FIGURE 2 A simplified pulse sequence diagram for a HSS in vivo acquisition showing the spectral-spatial excitation (0-0.01 seconds), z phase encode (0.01 seconds, slice), and HSS readout (0.01 seconds—end)

state identical to an N-shot spiral at $k_r = k_{\text{trans}}$, as shown in Figure 1, resulting in a smooth transition between the two densities without violating $G_{\max}$ or $S_{\max}$. The pseudo-code describing this is shown in the appendix.

3 | METHODS

3.1 | Sequence design

The proposed sequence is a 3D HSS with spectral-spatial excitation, centric phase encodes in the z-direction, and a hybrid spiral readout with rewind. A simplified representation of the sequence is shown in Figure 2.

A spectral-spatial excitation scheme was used to provide spectrally selective excitation within the volume of interest, while minimizing excitation outside of the volume of interest, in order to preserve the pool of hyperpolarized magnetization circulating in the animal, as our coil could not provide enough spatial localization by itself. As described previously,[31] the spectral-spatial excitation pulses were designed under the RF excitation k-space formalism with zipper correction.[32] Subpulses under a Gaussian envelope were designed with the Shinnar-Le-Roux algorithm,[33] with a time-bandwidth product of 3 in the spectral domain and 9 in the spatial domain, and zero amplitude on negative gradient lobes to produce a fly-back pulse. The scheme was originally designed to be slew-rate ($S_{\max}$) limited rather than gradient ($G_{\max}$) limited, as we have empirically found at both 7T and 3T that waveforms played at $S_{\max}$ were reproduced with significantly better fidelity than those at $G_{\max}$,[31] when measured by the method proposed by Duyn et al.[34]

The pulse was 9 ms long, possessed 37 sub-lobes each of duration 246 μs, corresponding to an excitation bandwidth of 240 Hz, and a stop-band of ∼2 kHz, sufficient to avoid every unwanted resonance in the spectrum of hyperpolarized [1-^{13}C]pyruvate at 7T, with an excitation bandwidth sufficiently large (3 ppm) to provide relative immunity to transmitting off-resonance and B_0 inhomogeneity. The slab thickness was 45.5 mm.

In the proposed HSS k-space encoding scheme, a single-shot and N-shot spiral were compounded together and rotated by $360/N°$ so that the central region of k-space was fully sampled every shot and the outer region was fully sampled every N shots. This allowed for a low spatial resolution image to be reconstructed every shot (single-shot HSS), giving maximum temporal resolution, or for N consecutive shots to be combined giving a higher spatial resolution, albeit at the cost of temporal resolution (full HSS). The spiral readouts were rotated by $360/N°$, as opposed to the golden angle, in order to maximize the signal-to-noise ratio of the reconstructed image when N shots were combined.[35] The sequence was implemented using a modified version of the Hargreaves variable density spiral algorithm[29] to generate the two spirals which are smoothly transitioned between.

3.2 | Image reconstruction

Image reconstruction was performed with custom software written in the Matlab programming language (Mathworks, Natick, MA, 2018b). It used the Berkeley Advanced Reconstruction Toolbox[36] implementation of the nonuniform Fourier transform (NUFFT) to reconstruct the data in the x-y plane. The k-space trajectory used in the NUFFT calculation was computed by correcting the prescribed gradients with a previously measured gradient impulse response function[37] and numerically integrating the result.

In this work, the bulk B_0 shift (which causes a "blurring" artifact in image space or "ringing" in the PSF[38] and is hard to avoid, since the pyruvate center frequency is not known accurately ahead of time) was corrected by a method similar to that used by Lau et al,[39] where the images were reconstructed with a range of different demodulation frequencies and the least blurred image taken; however, in this work, the selection was done manually, rather than with an automated approach. While this demodulation was necessary from an image quality point of view it also provided an estimate of the actual ^{13}C center frequency, validating that this parameter was set correctly at acquisition.

3.3 | Digital phantom

To provide initial validation of the sequence, single-shot, multiple-shot and HSS ^{13}C acquisitions were simulated with a synthetic brain phantom.[40] The simulated scanner had $G_{max} = 500\,mT/m$, $S_{max} = 536\,mT/m/ms$ and a bandwidth of 62.5 kHz. The multiple-shot and HSS trajectories had three interleaves. The trajectories were calculated to achieve an x/y resolution of 1 mm (single-shot HSS 5 mm) and FOV of 60 mm. After calculation, the trajectories were truncated to the length of the multiple-shot spiral (15.9 ms) for comparison with equal readout time, giving resolutions for each method of: single-shot HSS 5 mm, full HSS 1.1 mm, single-shot spiral 1.9 mm and multiple-shot spiral 1 mm. The T_2^* of the simulated phantom was chosen to be 19 ms as a representative value for hyperpolarized pyruvate in vivo and the simulated excitation flip angle, for depletion of the pool of hyperpolarized magnetization, was 3°.

Two factors affecting the quality of the reconstructed images were simulated: receive off-resonance and noise. Receive off-resonance was simulated by multiplying the simulated FID by a phase term corresponding to 0-100 Hz off-resonance. Noise was simulated by injecting random Gaussian noise, with a full width at half maximum (FWHM) of 0-10% the maximum FID intensity, into the simulated FID prior to reconstruction. A structural similarity index (SSIM) was calculated for each reconstruction, using the ground truth phantom as a reference, to assess the reconstructed image quality.

3.4 | ^1H phantom

Further validation of the sequence was performed with ^1H phantom measurements. The resolution phantom consisted of a tube containing Lego pieces filled with a Ferumoxytol solution (elemental iron concentration of 30 μg/mL) to give a T_2^* of 12.1 ms. The scanner was a Varian 7T DDR system with $G_{max} = 1000\,mT/m$, $S_{max} = 5000\,mT/m/ms$, coupled with a 72 mm dual-tuned proton/carbon birdcage volume coil. A 5° sinc pulse with duration 1000 μs and slab thickness 45.5 mm was used for the excitation and the bandwidth was set to 250 kHz.

Single-shot, multiple-shot, and HSS 3D acquisitions were acquired for comparison. The multiple-shot spiral and full HSS trajectories each had three interleaves. The trajectories were designed with a FOV of 80 × 80 × 45.5 mm and resolution of 0.5 × 0.5 × 1.4 mm with the single-shot HSS reconstruction giving a resolution of 2.5 × 2.5 × 1.4 mm. The trajectories were then truncated to the same readout time (14.8 ms), corresponding to a full HSS resolution of 0.8 mm (multi-shot spiral 0.7 mm, single-shot spiral 1.3 mm). 32 z phase encode steps were used.

In addition to the spiral acquisitions, a 3D gradient echo sequence was used to acquire a high-resolution ground truth image. The FOV was 80 × 80 × 45.5 mm and the resolution 0.4 × 0.4 × 1.4 mm. SSIM indices were calculated for each spiral reconstruction over a region of interest (indicated in Figure 4) and an intensity profile was plotted through the phantom for each acquisition.

3.5 | Preclinical imaging

Preclinical proof-of-concept experiments were performed on a Varian 7T DDR system with $G_{max} = 1000\,mT/m$, $S_{max} = 5000\,mT/m/ms$, with an actively detuned transmit/surface receive setup consisting of a 72 mm dual-tuned proton/carbon birdcage volume coil with a 40 mm two-channel ^{13}C surface receive array with an integrated preamp (Rapid Biomedical GmbH, Rimpar, Germany).

Approximately 40 mg of [1-^{13}C]pyruvic acid doped with 15 mM OX063 trityl radical and 3 μL of a 1-in-50 dilution of Dotarem (Guerbet Laboratories Ltd) gadolinium chelate was polarized and dissoluted in a prototype polarizer as described previously.[41] Male Wistar rats were anesthetized with 2% isoflurane in 90%O_2, 10%N_2O, placed prone onto the imaging coil in a home-built preclinical imaging cradle, and injected with 2 ml of 80 mM hyperpolarized [1-^{13}C] over approximately 20 seconds.

A thermally polarized 5 M ^{13}C urea phantom was included next to the animal to provide a carbon frequency reference. Three-dimensional, cardiac-gated volume shimming was performed using the previously mapped behavior of the magnet's shim set and a spherical harmonic cardiac auto-shimming algorithm as described previously.[42] The ^{13}C center frequency was set by identifying the carbon resonant frequency of the urea phantom, and applying a constant offset of 296 Hz (3.95 ppm). This consisted of the B_0 variation between the urea phantom and the heart (estimated from previously performed ΔB_0 maps), the known chemical shift difference from ^{13}C urea to [1-^{13}C], and empirical optimizations. The ^{13}C center frequency was verified during reconstruction as described in the image reconstruction section.

Once injected with the hyperpolarized [1-^{13}C] solution, three rats were imaged using the proposed sequence, consisting of a spectral-spatial excitation and a cardiac-gated (one shot per RR interval) three interleaf HSS readout scheme. The imaging parameters, for the first two rats, consisted of a readout bandwidth of 250 kHz, a FOV of 120 × 120 × 45.5 mm, 12 z phase encode steps, a resolution of 2 × 2 × 3.8 mm and a single-shot HSS resolution of 10 × 10 × 3.8 mm, the nominal minimum TR (time for 1 rotation angle for one metabolite) before gating was 212.4 ms. The excitation flip angles were: pyruvate 3°, bicarbonate 20°, and lactate 20°. One of these rats was injected with hyperpolarized [1-^{13}C] a second

time in a single session, and imaged with a single-shot spiral with the same FOV and resolution as the full HSS acquisition and a nominal TR of 352.0 ms before gating.The third rat was imaged with a readout bandwidth of 62.5 kHz, a FOV of 60 × 60 × 45.5 mm, 12 z phase encode steps, a resolution of 1 × 1 × 3.8 mm and a single-shot HSS resolution of 5 × 5 × 3.8 mm.

After the hyperpolarized imaging, a set of anatomical images were acquired using a gradient echo cine sequence described previously,[43] with the same slice thickness and FOV as the hyperpolarized data.

All experiments were performed in accordance with relevant UK legislation (with personal, project and institutional licenses granted under the Animals (Scientific Procedures) Act 1986), and were subject to local ethical review and an independent cost-benefit analysis.

4 | RESULTS

4.1 | Digital phantom

The results of the digital phantom experiment are summarized in Figure 3. With no injected noise or simulated off-resonance, the full HSS and multiple-shot spiral reconstructions have a similar SSIM metric when using the ground truth as a reference image. The single-shot reconstruction had a lower SSIM than either the multiple-shot or full HSS reconstructions and the single-shot HSS reconstruction had the lowest SSIM. This broadly follows the theoretical resolution achieved by each readout in the acquisition time, although the multiple-shot spiral would have been expected to perform better than full HSS, without the influence of T_2^*, the depletion of the hyperpolarized magnetization pool and oversampling of the center of k-space for full HSS.

As noise is added the SSIM for all reconstructions decreases, full HSS, multiple-shot, and single-shot, which all have equal readout time, decrease at roughly the same rate. As the injected noise increases, the single-shot spiral performs better than either the full HSS or multiple-shot spiral. Single-shot HSS, with a shorter readout time than the other reconstructions, decreases less quickly than the other methods so that it has the highest SSIM once the noise FWHM reaches around 6% the maximum value of the FID.

The SSIM of all reconstructions decreases with increasing off-resonance. The single-shot HSS reconstruction decreases much less quickly than the other readouts, due to its shorter length; however, there are differences in the other reconstructions, which each have equal readout time. Of the multiple-shot, single-shot, and full HSS reconstructions, the multiple-shot image quality degrades the least quickly with added off-resonance. Initially, the full HSS reconstruction out performs the single-shot spiral; however, at greater than 61.5 Hz, this reverses and full HSS gives the lowest SSIM of all the reconstructions.

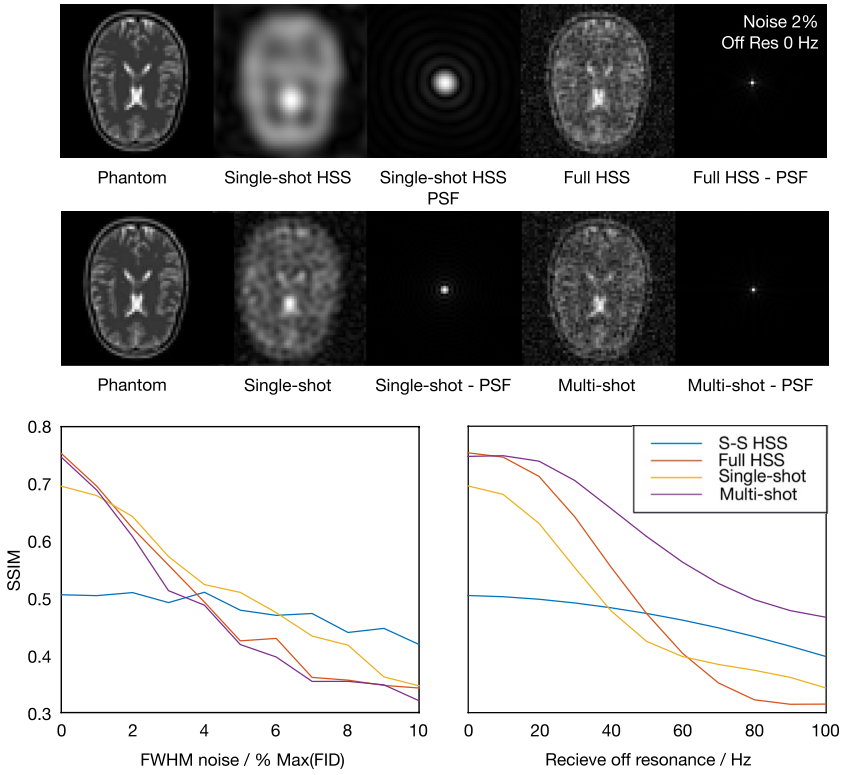

FIGURE 3 Top: Sample images showing reconstructed HSS, single-shot, and multiple-shot acquisitions and a ground truth digital phantom with Gaussian noise (FWHM of noise 2% maximum value of FID) injected into the FID. Bottom: SSIM of the reconstructed images, with the digital phantom as ground truth, as a function of injected noise and simulated receive off-resonance

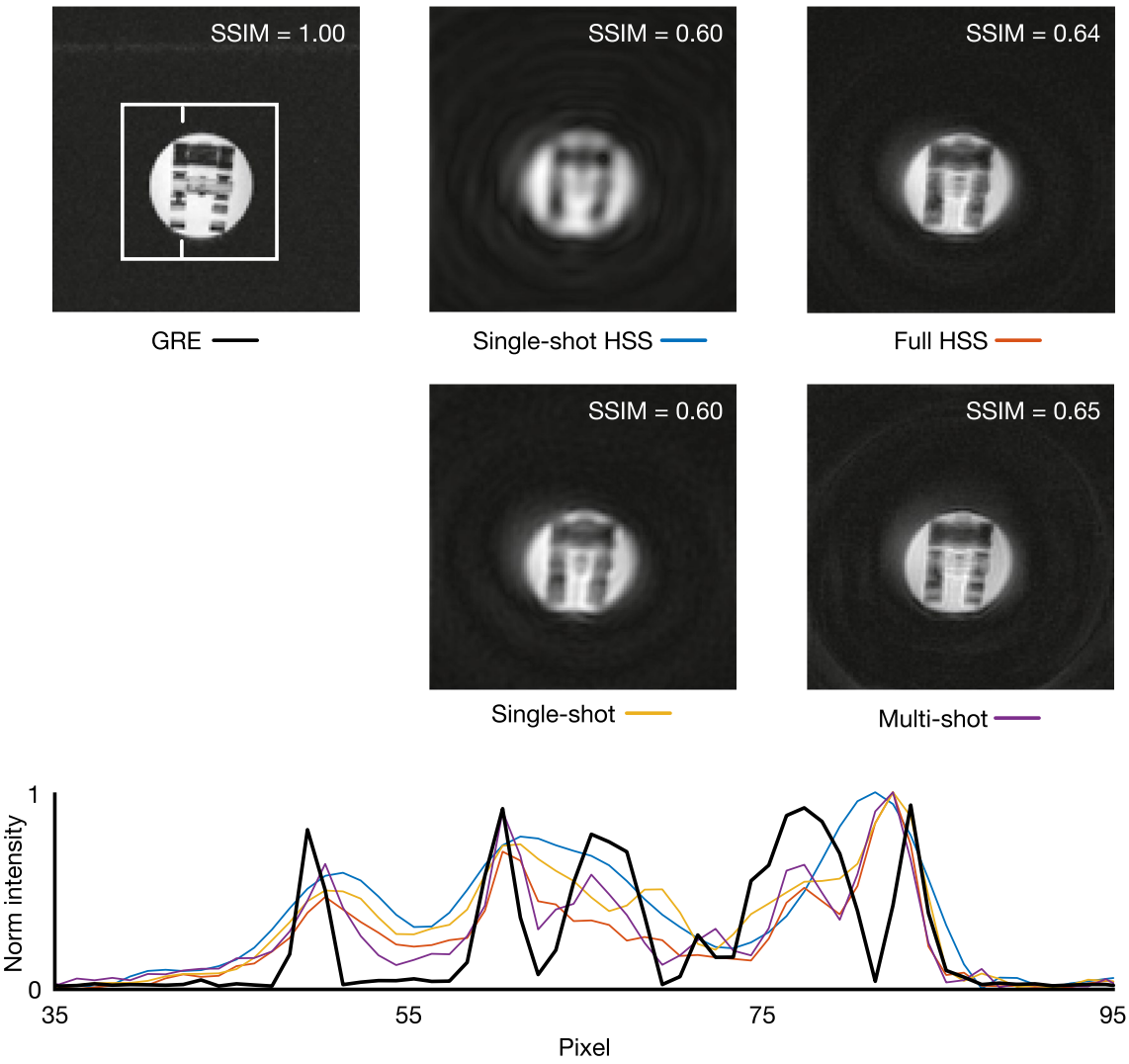

FIGURE 4 Top: Reconstructed images of a resolution phantom ($T_2^* = 12$ ms) with structural similarity index, over the area in the white box, with the gradient echo (GRE) acquisition shown as reference, in the top right of each image. Bottom: Normalized line plot through each of the reconstructed images. The position of the line is denoted by the white notches in the gradient echo image

4.2 | ^{1}H phantom

Reconstructed images and a line plot through the ^{1}H phantom are shown in Figure 4. The structural similarity of the reconstructed images to a reference gradient echo image were calculated and broadly followed the expected trend of decreasing SSIM with decreasing resolution. The single-shot HSS reconstruction had a SSIM equal to the single-shot spiral despite achieving a lower resolution potentially due to the shorter readout time reducing the measured noise.

The line plot through the ^{1}H phantom illustrates the trend quantified by the SSIM indices. The multiple-shot and full HSS reconstructions show more definition than the single-shot or single-shot HSS reconstructions which are comparatively blurred.

Significantly, the HSS acquisition achieved similar image quality to the multiple-shot spiral, when a full reconstruction was performed with the same number of shots, and when only a single-shot was used it produced images of comparable quality to the single-shot spiral while matching its temporal resolution.

4.3 | Preclinical imaging

The results of the preclinical hyperpolarized experiments are illustrated in Figures 5 and 6. The line plot in Figure 5 shows the resolution trade-off made by the HSS sequence. The single-shot HSS reconstruction has a visibly lower spatial resolution than the single-shot spiral; however, the full HSS reconstruction, separated the left and right ventricles, demonstrating its higher resolution. Figure 5 also shows a time-course of pyruvate signal-to-noise ratio for the same hyperpolarized datasets. In this example, the single-shot HSS reconstruction captured dynamic information about the system, particularly the bolus arrival and second pass of the pyruvate, while the full HSS reconstruction lacked the temporal resolution to do so. Figure 6

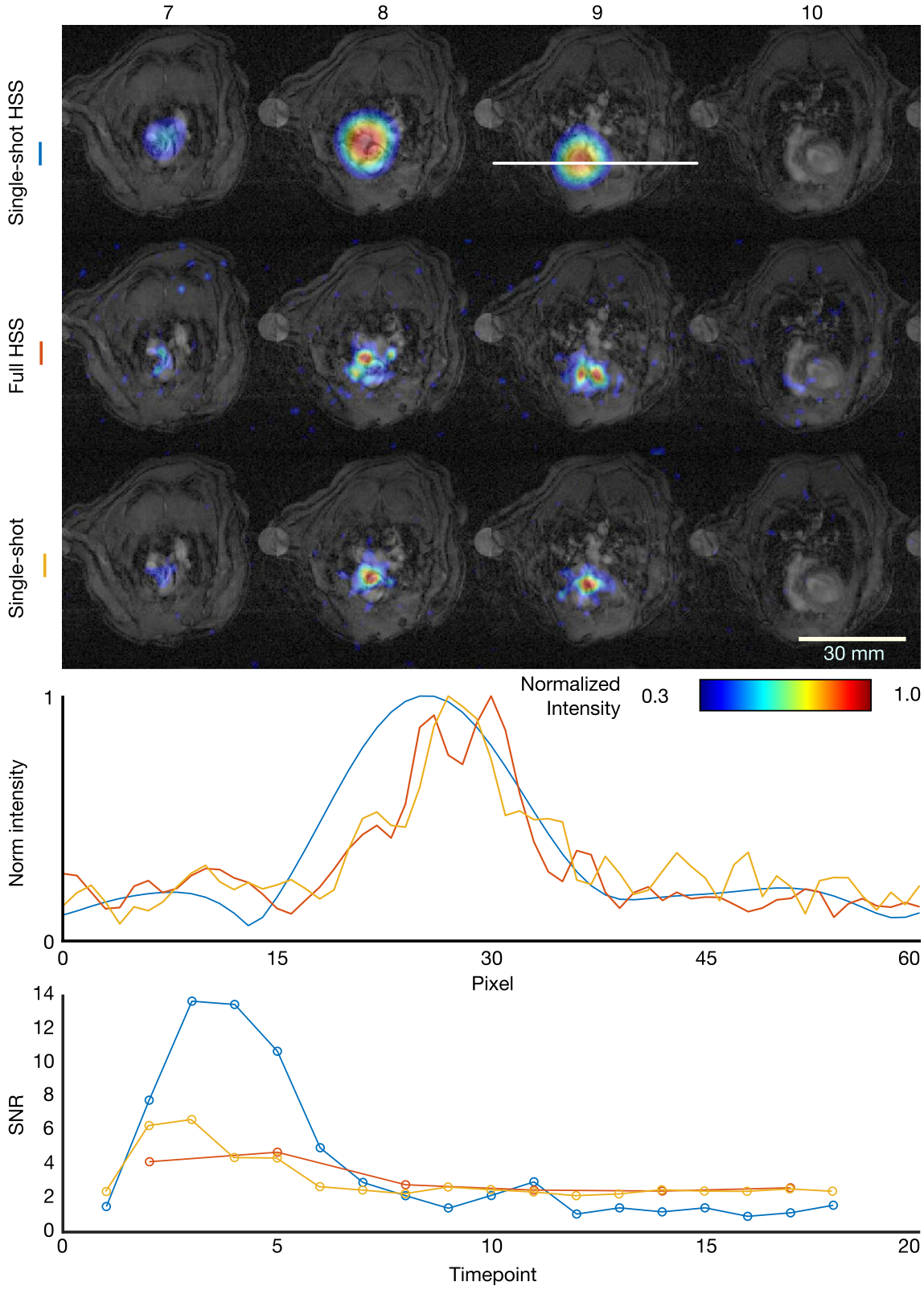

FIGURE 5 Top: Axial slices 7-10 of HSS and single-shot ^{13}C acquisitions of a rat injected with hyperpolarized [1-^{13}C] overlaid on to matched ^{1}H anatomical images, excited at the pyruvate resonant frequency. Middle: Line plots through slice 9 of each reconstruction in the position indicated by the white line in the single-shot HSS image. Bottom signal-to-noise ratio of pyruvate in the rat heart (Figure 5, slice 9) as a function of acquisition timepoint for single-shot and full reconstructions of a HSS acquisition in addition to a single-shot acquisition

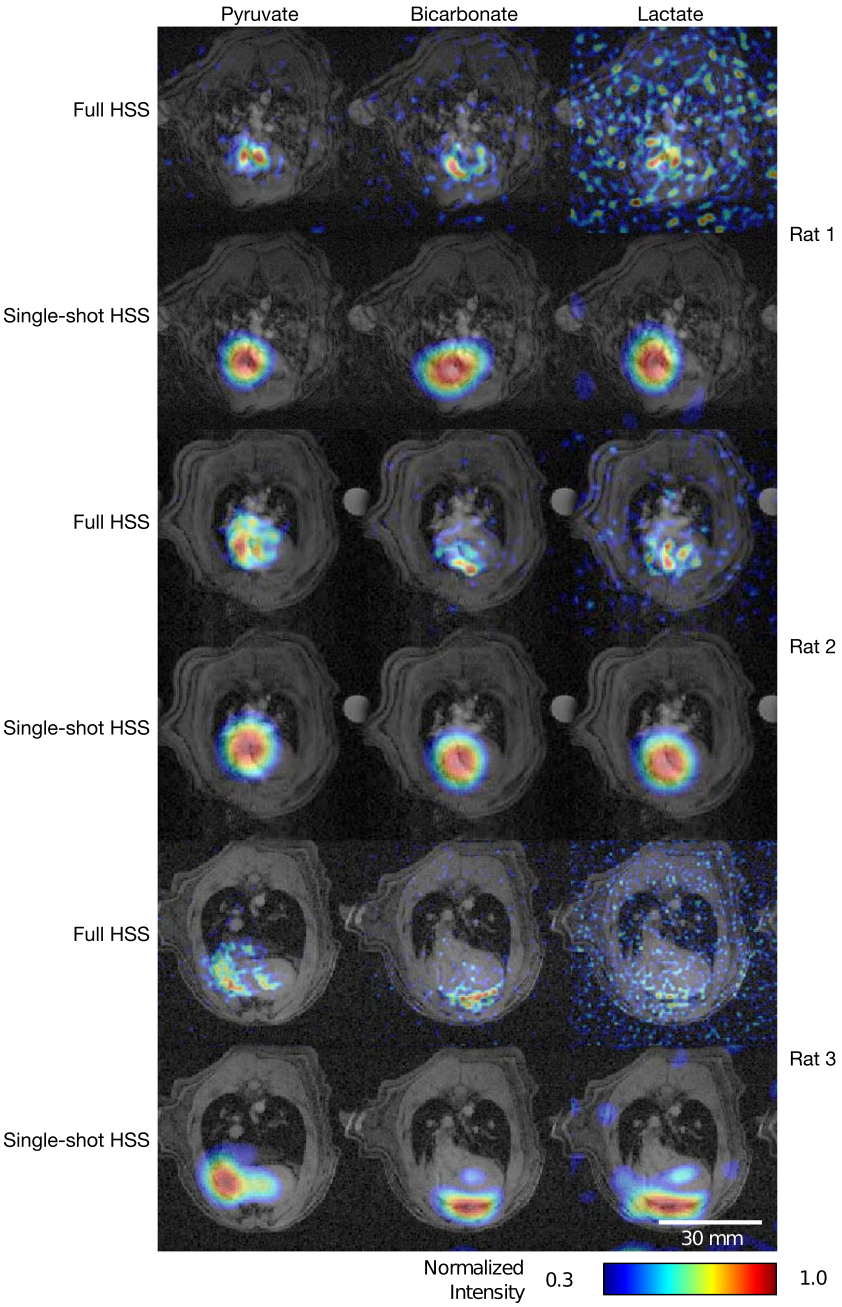

FIGURE 6 Pyruvate, bicarbonate, and lactate HSS images for the rat shown in Figure 5 (Rat 1) in addition to two additional rats, one (rat 2) imaged with the same imaging parameters and the other (rat 3) with different parameters (bandwidth = 62.5 kHz, FOV = 60 mm, full HSS resolution = 1 mm, single-shot HSS resolution = 5 mm)

shows pyruvate, bicarbonate, and lactate metabolic images acquired with the HSS sequence for three rats, two imaged with the same imaging parameters and a third with 4× lower bandwidth, 0.5× FOV and 2× resolution. In all three sets of images, the signal is localized to anatomically plausible regions, with the full HSS reconstruction revealing anatomical detail, which was not resolved by the single-shot HSS reconstruction.

5 | DISCUSSION

In this work, we demonstrated the feasibility of the HSS pulse sequence for use in hyperpolarized [1-^{13}C] cardiac imaging. We also explored the trade-offs which inform the choice of spiral readout when designing hyperpolarized studies. Due to the inherent difficulty in measuring image quality for hyperpolarized reconstructions, as there is no ground truth, we performed validation work in both digital and ^{1}H phantoms in addition to demonstrating feasibility in a preclinical rat model.

The main features of the sequence, and the trade-offs it makes, are illustrated clearly by the digital phantom simulation data presented here. In the ideal case, the full HSS reconstruction achieved similar image quality to a multiple-shot readout with the same readout duration, while retaining the ability to reconstruct a low resolution image from a single shot. The main trade-off of the sequence, the single-shot HSS resolution, is clearly demonstrated by its lower SSIM than the single-shot spiral simulation.

Furthermore, the simulated full HSS sequence had broadly similar robustness to noise compared to both single and multiple-shot readouts. However, as injected noise increased, the single-shot spiral outperformed the full HSS and multiple shot readouts, potentially due to it incorporating less noise from a shorter total (across all interleaves) readout duration.

Of the equal readout length simulations (ie, not single-shot HSS), the multiple-shot simulation had the greatest resilience to off-resonance effects, with the full HSS simulation initially performing better than the single-shot simulation before degrading more quickly. Since the readout times were the same, it cannot account for this difference; however, we believe that it could potentially be in part due to the re-gridding process in the NUFFT and the relative amount of time spent during the readout at high spatial frequencies away from the center of k-space.

The ^{1}H phantom provided quantitative validation of the simulations in a controlled experimental system. While closely mirroring the digital phantom simulations, the similarity in SSIM metric between the single-shot spiral and single-shot HSS acquisition was surprising; however, from the line plot through the phantom, it is clear that the single-shot spiral did achieve a higher spatial resolution despite a poorer similarity to the reference image, potentially due to greater noise.

The preclinical results reported here are qualitatively consistent with the digital and ^{1}H phantom validation data, and further illustrate the characteristics of the sequence. The improved resolution of a full HSS acquisition over a single-shot spiral with equal prescribed resolution is demonstrated by the line plot through the heart shown in Figure 5, where the pyruvate signal is clearly localized to the two ventricles, unlike for the single-shot spiral. In addition, the time-course data shown in Figure 5 demonstrates that the single-shot HSS reconstruction is able to capture appreciably more of the dynamics of the system, necessary for kinetic modeling, than the full HSS reconstruction, albeit with a lower spatial resolution than a single-shot spiral with the same temporal resolution. It is also worth noting that for a single-shot HSS reconstruction, or single-shot spiral each timepoint is reconstructed from consecutive readouts (ie, for 12 z phase encodes and a heart rate of 400 bpm, over 1.8 seconds), unlike for a multi-shot spiral, or full HSS, where each timepoint is a moving average of N shots which may be temporally separated by readouts for other metabolites, making data analysis for kinetic modeling more challenging.

Figure 6 shows pyruvate, bicarbonate, and lactate images reconstructed from the same data shown in Figure 5, as well as images acquired from two further rats. Image quality across the datasets is comparable to prior work imaging the rat heart at 7T.[31] Furthermore, the alternative set of imaging parameters, used for rat 3, resulted in noticeably improved image quality, with better delineation of the myocardium. However, the drop-off in signal toward the rear of the heart, particularly noticeable in the bicarbonate images, due to the sensitivity profile of the ^{13}C surface receive coil, demonstrates the challenge of hyperpolarized imaging of the rat heart at 7T. These images demonstrate the reproducibility of the sequence, as well as the feasibility of combining the HSS readout with a spectral-spatial excitation, which allows spatial details, such as the bicarbonate signal from the myocardium, to be resolved while maintaining temporal resolution and spectral selectivity.

Overall, the HSS pulse sequence provides an attractive compromise between spatial and temporal resolution for hyperpolarized ^{13}C MRI, by making a spatial resolution trade-off compared to a traditional multiple-shot acquisition for the ability to reconstruct as a single or multiple-shot spiral from a single acquisition. As such, it forms an attractive candidate for use in clinical imaging, where the benefits of the increased resolution it can provide, compared to a single-shot spiral, would be appreciated, particularly when imaging conditions with spatially localized metabolic dysregulation such as myocardial infarction.

6 | CONCLUSION

Hyperpolarized ^{13}C imaging of the human heart has been demonstrated with a single-shot spiral readout, however the maximum resolution, for a given FOV, this approach can achieve is fundamentally limited by T_2^* decay. This limitation may negatively impact the prospects of developing diagnostic methods for conditions such as ischemia of the heart, which have shown promise in a preclinical setting, that rely on resolving tissue metabolism heterogeneity. The HSS sequence aims to address this limitation of spiral imaging by making a spatial resolution trade-off compared to a traditional multiple-shot acquisition for the ability to reconstruct each shot individually. This allows for multiple-shot images to be reconstructed at a resolution greater than is achievable with a single-shot acquisition, while offering the option to reconstruct images at the temporal resolution of a single-shot spiral, with the trade-off of reduced spatial resolution compared to a standard single-shot sequence.

The experiments presented in this work demonstrate the capabilities of the sequence, as well as its relative trade-offs, and suggest the benefits it may have going forward into clinical translation for hyperpolarized ^{13}C imaging. In our future work, we initially plan to further develop the sequence by implementing a B_0 inhomogeneity correction to reduce the impact, identified by simulations, of off-resonance effects in vivo before implementing the sequence on a clinical system for use in human hyperpolarized ^{13}C cardiac studies.

ACKNOWLEDGMENTS

This work was supported by funding from the Engineering and Physical Sciences Research Council (EPSRC) and Medical Research Council (MRC) [grant number EP/L016052/1]. All authors acknowledge the support of the British Heart Foundation (Senior Fellowship ref. FS/14/17/30634, and the Oxford BHF Centre for Research Excellence ref. RE/13/1/30181) and the support of the UK NIHR. JYCL acknowledges the funding from the NIHR Oxford Biomedical Research Centre and support from the Fulford Junior Research Fellowship at Somerville College. All authors would like to acknowledge the NHS National Institute for Health Research Oxford Biomedical Research Centre programme. The views expressed are those of the authors and not necessarily those of the NIHR or the Department of Health and Social Care. JJM acknowledge the financial support by a Novo Nordisk Postdoctoral Fellowship scheme run in conjunction with the University of Oxford, and also by St Hugh's and Wadham college in the University of Oxford.

ORCID

Andrew Tyler https://orcid.org/0000-0001-7013-2648
Justin Y. C. Lau https://orcid.org/0000-0001-7316-811X
Kerstin N. Timm https://orcid.org/0000-0001-9136-7518
Damian J. Tyler https://orcid.org/0000-0002-0780-8905
Jack J. Miller http://orcid.org/0000-0002-6258-1299

TWITTER

Jack J. Miller @DrJackMiller

REFERENCES

1. Golman K, Petersson JS. Metabolic imaging and other applications of hyperpolarized $^{13}C^{1}$. *Acad Radiol*. 2006;13:932–942.
2. Golman K, Zandt RI, Lerche M, Pehrson R, Ardenkjaer-Larsen JH. Metabolic imaging by hyperpolarized ^{13}C magnetic resonance imaging for in vivo tumor diagnosis. *Cancer Res*. 2006;66:10855–10860.
3. Gallagher FA, Kettunen MI, Day SE, et al. Magnetic resonance imaging of pH in vivo using hyperpolarized ^{13}C-labelled bicarbonate. *Nature*. 2008;453:940–943.
4. Nelson SJ, Kurhanewicz J, Vigneron DB, et al. Metabolic imaging of patients with prostate cancer using hyperpolarized [1-^{13}C]. *Sci Trans Med*. 2013;5:198ra108.
5. Cunningham CH, Lau JYC, Chen AP, et al. Hyperpolarized ^{13}C metabolic MRI of the human heart: initial experience. *Circulation Res*. 2016;119:1177–1182.
6. Miloushev VZ, Granlund KL, Boltyanskiy R, et al. Metabolic imaging of the human brain with hyperpolarized ^{13}C pyruvate demonstrates ^{13}C lactate production in brain tumor patients. *Cancer Res*. 2018;78:3755–3760.
7. Grist JT, McLean MA, Riemer F, et al. Quantifying normal human brain metabolism using hyperpolarized [1-^{13}C] and magnetic resonance imaging. *NeuroImage*. 2019;189:171–179.
8. Stødkilde-Jørgensen H, Laustsen C, Hansen ESS, et al. Pilot study experiences with hyperpolarized [1-^{13}C] pyruvate MRI in pancreatic cancer patients. *J Magn Reson Imaging*. 2019. https://doi.org/10.1002/jmri.26888.
9. Rider OJ, Apps A, Miller JJ, et al. Non-invasive in vivo assessment of cardiac metabolism in the healthy and diabetic human heart using hyperpolarized ^{13}C MRI. *Circulation Res*. 2020. https://www.ahajournals.org/doi/abs/10.1161/CIRCRESAHA.119.316260
10. Lau AZ, Chen AP, Barry J, et al. Reproducibility study for free-breathing measurements of pyruvate metabolism using hyperpolarized ^{13}C in the heart. *Magn Reson Med*. 2013;69:1063–1071.
11. Geraghty BJ, Lau JYC, Chen AP, Cunningham CH. Accelerated 3D echo-planar imaging with compressed sensing for time-resolved hyperpolarized ^{13}C studies. *Magn Reson Med*. 2017;77:538–546.
12. Gordon JW, Bok RA, Cao P, et al. Pulse sequence considerations for quantification of pyruvate-to-lactate conversion k^{PL} in hyperpolarized 13C imaging. *NMR Biomed*. 2019:e4052. https://doi.org/10.1002/nbm.4052.
13. Hill DK, Orton MR, Mariotti E, et al. Model free approach to kinetic analysis of real-time hyperpolarized ^{13}C magnetic resonance spectroscopy data. *PLOS ONE*. 2013;8:e71996.
14. Durst M, Koellisch U, Frank A, et al. Comparison of acquisition schemes for hyperpolarised ^{13}C imaging. *NMR Biomed*. 2016;28:715–725.
15. Mayer D, Yen Y-F, Tropp J, Pfefferbaum A, Hurd RE, Spielman DM. Application of sub-second spiral chemical shift imaging to real-time multislice metabolic imaging of the rat in vivo after injection of hyperpolarized $^{13}C_1$-pyruvate. *Magn Reson Med*. 2009;62:557–564.
16. Mayer D, Yen Y-F, Levin YS, et al. In vivo application of sub-second spiral chemical shift imaging (CSI) to hyperpolarized ^{13}C metabolic imaging: comparison with phase-encoded CSI. *J Magn Reson*. 2010;204:340–345.
17. Lau AZ, Chen AP, Hurd RE, Cunningham CH. Spectral-spatial excitation for rapid imaging of DNP compounds. *NMR Biomed*. 2011;24:988–996.
18. Wiesinger F, Weidl E, Menzel MI, et al. IDEAL spiral CSI for dynamic metabolic MR imaging of hyperpolarized [1-^{13}C] pyruvate. *Magn Reson Med*. 2012;68:8–16.
19. Wang J, Wright AJ, Hu D-E, Hesketh R, Brindle KM. Single shot three-dimensional pulse sequence for hyperpolarized ^{13}C MRI. *Magn Reson Med*. 2017;77:740–752.
20. Miller JJ, Grist JT, Serres S, et al. ^{13}C pyruvate transport across the blood-brain barrier in preclinical hyperpolarised MRI. *Sci Rep*. 2018;8:15082.
21. Lau AZ, Chen AP, Cunningham CH. Imaging the circumferential hyperpolarized ^{13}C-bicarbonate distribution in the normal heart. *Proc Int Soc Mag Reson Med*. 2019;27:0256.
22. Meyer CH, Hu BS, Nishimura DG, Macovski, A. Fast spiral coronary artery imaging. *Magn Reson Med*. 1992;28:202–213.
23. Spielman DM, Pauly JM, Meyer CH. Magnetic resonance fluoroscopy using spirals with variable sampling densities. *Magn Reson Med*. 1995;34:388–394.
24. Liao J-R, Pauly JM, Brosnan TJ, Pelc NJ. Reduction of motion artifacts in cine MRI using variable-density spiral trajectories. *Magn Reson Med*. 1997;37:569–575.

25. Tsai C-M, Nishimura DG. Reduced aliasing artifacts using variable-density k-space sampling trajectories. *Magn Reson Med*. 2000;43:452–458.
26. Glover GH. Simple analytic spiral k-space algorithm. *Magn Reson Med*. 1999;42:412–415.
27. Kim D-H, Adalsteinsson E, Spielman DM. Simple analytic variable density spiral design. *Magn Reson Med*. 2003;50:214–219.
28. Chang C, Glover GH. Variable-density spiral-in/out functional magnetic resonance imaging. *Magn Reson Med*. 2011;65:1287–1296.
29. Lee JH, Hargreaves BA, Hu BS, Nishimura DG. Fast 3D imaging using variable-density spiral trajectories with applications to limb perfusion. *Magn Reson Med*. 2003;50:1276–1285.
30. Hargreaves B. *Spin-manipulation methods for efficient magnetic resonance imaging* [PhD thesis]. Department of Electrical Engineering, Stanford University, 2001.
31. Miller JJ, Lau AZ, Teh I, et al. Robust and high resolution hyperpolarized metabolic imaging of the rat heart at 7 T with 3D spectral-spatial EPI. *Magn Reson Med*. 2016;75:1515–1524.
32. Lau AZ, Chen AP, Ghugre NR, etal. Rapid multislice imaging of hyperpolarized ^{13}C pyruvate and bicarbonate in the heart. *Magn Reson Med*. 2010;64:1323–1331.
33. Shinnar M, Eleff S, Subramanian H, Leigh JS. The synthesis of pulse sequences yielding arbitrary magnetization vectors. *Magn Reson Med*. 1989;12:74–80.
34. Duyn JH, Yang Y, Frank JA, van der Veen JW. Simple correction method for k-space trajectory deviations in MRI. *J Magn Reson*. 1998;132:150–153.
35. Winkelmann S, Schaeffter T, Koehler T, Eggers H, Doessel O. An optimal radial profile order based on the golden ratio for time-resolved MRI. *IEEE Trans Med Imaging*. 2007;26:68–76.
36. Uecker M, Ong F, Tamir JI, et al. Berkeley advanced reconstruction toolbox. *Proc Int Soc Mag Reson Med*. 2015;23:2486.
37. Vannesjo SJ, Haeberlin M, Kasper L, et al. Gradient system characterization by impulse response measurements with a dynamic field camera. *Magn Reson Med*. 2013;69:583–593.
38. Block KT, Frahm J. Spiral imaging: a critical appraisal. *J Magn Reson Imaging*. 2005;21:657–668.
39. Lau AZ, Miller JJ, Robson MD, Tyler DJ. Cardiac perfusion imaging using hyperpolarized ^{13}C urea using flow sensitizing gradients. *Magn Reson Med*. 2016;75:1474–1483.
40. Guerquin-Kern M, Lejeune L, Pruessmann KP, Unser M. Realistic analytical phantoms for parallel magnetic resonance imaging. *IEEE Trans Med Imaging*. 2012;31:626–636.
41. Ardenkjær-Larsen JH, Fridlund B, Gram A, et al. Increase in signal-to-noise ratio of >10 000 times in liquid-state NMR. *Proc Nat Acad Sci*. 2003;100:10158–10163.
42. Schneider JE, Barnes H, Neubauer S, Jezzard P. Automated-shim approach to facilitate ^{1}H-MRS in mouse hearts in vivo. *Proc Int Soc Mag Reson Med*. 2009;17:1782.
43. Schneider JE, Cassidy PJ, Lygate C, et al. Fast, high-resolution in vivo cine magnetic resonance imaging in normal and failing mouse hearts on a vertical 11.7 T system. *J Magn Reson Imaging*. 2003;18:691–701.

How to cite this article: Tyler A, Lau JYC, Ball V, et al. A 3D hybrid-shot spiral sequence for hyperpolarized ^{13}C imaging. *Magn Reson Med*. 2021;85:790–801. https://doi.org/10.1002/mrm.28462

APPENDIX A
HSS READOUT ALGORITHM

Pseudo-code, describing the algorithm used to generate the spiral trajectories in this work, is shown below. The algorithm was modified from an existing VDS design algorithm[29] and implemented in the C programming language

$N \leftarrow N;$

$\ddot{k}_r, \ddot{\theta}, \dot{k}_r, \dot{\theta}, k_r, \theta \leftarrow 0;$

while $k_r < k_{trans}$ **do**

  calculate next $\ddot{k}_r, \ddot{\theta}, \dot{k}_r, \dot{\theta}, k_r, \theta;$

end

$\dot{k}_{\text{trans}} \leftarrow \dot{k}_r;$

$\ddot{k}_r, \ddot{\theta}, \dot{k}_r, \dot{\theta}, k_r, \theta \leftarrow 0;$

$N \leftarrow 1;$

while $k_r < k_{trans}$ **do**

  calculate next $\ddot{k}_r, \ddot{\theta}, \dot{k}_r, \dot{\theta}, k_r, \theta;$

  output $\ddot{k}_r, \ddot{\theta}, \dot{k}_r, \dot{\theta}, k_r, \theta;$

end

$N \leftarrow N;$

$\dot{k}_r \leftarrow \dot{k}_{\text{trans}};$

while $k_r < k_{max}$ **do**

  calculate next $\ddot{k}_r, \ddot{\theta}, \dot{k}_r, \dot{\theta}, k_r, \theta;$

  output $\ddot{k}_r, \ddot{\theta}, \dot{k}_r, \dot{\theta}, k_r, \theta;$

end

The algorithm begins by calculating $\dot{k}_{\text{trans}}$ (the first while loop), before resetting and calculating the single-shot trajectory up to $k_r = k_{\text{trans}}$ (the second while loop), at which point N is set to the number of shots in the multi-shot region and $\dot{k}_r$ is set to $\dot{k}_{\text{trans}}$. After which, the algorithm proceeds to calculate the multi-shot portion of the trajectory (the third while loop).